First-Principles Equation-of-State Table of Silicon and Its Effects on High-Energy-Density Plasma Simulations

Introduction

As one of the most-abundant elements on Earth, silicon is important to many different fields ranging from the semiconductor industry,[1] geophysics,[2] photovoltaics,[3] planetary and astrophysics,[4–6] to inertial confinement fusion (ICF) physics studies.[7–9] For ICF applications, silicon has been used as a dopant to ablators in indirect-drive ICF target designs.[10] It has also been applied to mitigate laser-imprint effects[11,12] and the two-plasmon–decay instability[13,14] for multilayer target designs in direct-drive ICF implosions.[15] For these high-energy-density (HED) applications, it is essential to know the properties of silicon under extreme conditions. The equation of state (EOS) of silicon is one of such intrinsic properties that are crucial to both ICF and geophysics applications since it is needed for hydrodynamic simulations of ICF implosions and for understanding the geophysics of the earth's outer core.[2]

The EOS studies of silicon under megabar (Mbar) pressures began in the 1960s (Ref. 16) using explosive drive. The principal Hugoniot measurements of silicon were continued in the 1970s and 1980s by different groups.[17,18] Many surprises were found in our understanding of the behavior of shocks in silicon. For instance, the elastic behavior of shocks was observed in silicon even at Mbar pressures.[19] Namely, the lattice reduction related to shock compression may occur only along the shock-propagation direction, instead of hydrostatical lattice-shrinking in all three dimensions. Furthermore, the measured optical emission from shocked silicon was found to be much lower than expected, which has been hypothesized to be caused by the unusually long electron–ion equilibration time in shocked silicon.[20–22] These abnormal phenomena have been observed in shock experiments up to ~6-Mbar pressures. What might occur for silicon pressures >10 Mbar remains to be seen. To the best of our knowledge, these anomalies observed in shocked silicon are not fully understood. To this end, a thorough understanding of silicon properties under HED conditions is necessary.

Theoretical investigations on shock compressions of silicon have been performed by classical molecular-dynamics methods,[23–25] quantum molecular dynamics simulations based on the density functional theory (DFT),[26–29] and path-integral Monte Carlo (PIMC) modeling.[27,29] Most of these studies have been devoted to the moderate-pressure regime of $P < 2$ Mbar, while the two most-recent first-principles calculations[27,29] extended the Hugoniot pressures from ~1 Mbar to over ~10 Gbar for the first time. These calculations combined the orbital-based–DFT Kohn–Sham molecular-dynamics (KSMD) method, the orbital-free–DFT molecular-dynamics (OFMD) method, and the PIMC simulation. All three first-principles calculations are in good agreement in predicting the principal Hugoniot of silicon, which was found to be ~20% softer than both the extensively used *SESAME*-EOS model[30] (Table 3810) and the quotidian equation-of-state (QEOS) model.[31] The predicted softening of silicon should have important implications for HED simulations of silicon plasmas. However, those calculations are concerned with only the plasma conditions along the principal Hugoniot. To study how such a softening behavior of silicon affects HED plasma simulations, we must expand our first-principles calculations to cover a wide range of off-Hugoniot plasma conditions.

In this article, we calculated the EOS for a wide range of silicon plasma conditions by using DFT-based molecular-dynamics simulations. To be specific, we have sampled silicon densities from $\rho = 0.001$ g/cm^3 to $\rho = 500$ g/cm^3 and temperatures from $T = 2000$ K to $T = 10^8$ K. Based on these *ab-initio* calculations, we have built a first-principles equation-of-state (FPEOS) table of silicon for ICF and HED applications. For off-Hugoniot conditions, we have investigated the differences in pressure and internal energy between FPEOS and *SESAME* EOS. Implementing the FPEOS table of silicon into the one-dimensional (1-D) hydrocode *LILAC*[32] and two-dimensional (2-D) hydrocode *DRACO*, we have tested its effects on HED plasma simulations of ICF implosions using a Si ablator. Comparisons with traditional *SESAME*-EOS simulations illustrated the need for more-accurate EOS tables to precisely design ICF and HED experiments.

The following sections: (1) describe the details of our first-principles calculations; (2) compare the FPEOS and *SESAME*

EOS for different isochoric plasma conditions (for completeness, the principal Hugoniot comparison is included, even though it has been reported elsewhere[29]); (3) present the effects of the FPEOS table on HED plasmas through *LILAC* simulations of ICF implosions using a silicon layer as the ablator; and (4) present our conclusions.

Molecular-Dynamics Simulations
Based on the Density Functional Theory

First-principles methods, such as DFT-based quantum molecular dynamics (QMD),[33–36] path-integral Monte Carlo,[37] and quantum Monte Carlo (QMC),[38,39] have been developed over the past decades to understand the properties of materials under extreme conditions. Two different versions of QMD have been implemented by the condensed-matter and HED physics communities. One uses the orbital-based Kohn–Sham formalism[40] with the finite-temperature density functional theory, in conjunction with the molecular-dynamics method for ion motion. The other is the orbital-free molecular-dynamics method,[41] which is based on the original DFT idea that the free energy of a many-electron system can be written as a function solely depending on the electron density. For most cases, the KSMD method has been proven to be an accurate and efficient method for calculating material properties under high compression at temperatures generally below the electron Fermi temperature T_F. It becomes impractical for high-temperature $(T > T_F)$ simulations because thermal excitation of electrons requires a large number of orbitals for convergence. The OFMD method is a natural extension of the KSMD method for high-T material simulations, even though it is not as accurate as KSMD. Nevertheless, the pressure difference between KSMD and OFMD calculations is still within ~1% in the overlapping regime of $T \sim T_F$ (valid for both methods), which is acceptable for general ICF/HED applications.

We have used the Vienna *ab initio* Simulation Package (VASP)[42–44] for KSMD simulations, in which electrons are treated quantum mechanically with a plane-wave finite-temperature DFT description. The electrons and ions of the material are in thermodynamic equilibrium with equal temperature $(T_e = T_i)$. The electron–ion Coulomb interaction is represented by a projector augmented-wave (PAW) pseudopotential with "frozen" 1s-core electrons. The electron exchange-correlation potential is described by the generalized-gradient approximation (GGA) with the Perdew–Burke–Ernzerhof (PBE) functional.[45] Under the Born–Oppenheimer approximation, the self-consistent electron density is first determined for an ion configuration. Then, the classical ions are moved by the combined electronic and ionic forces, using Newton's equation.

This molecular-dynamics procedure is repeated for thousands of time steps from which the thermodynamic EOS quantities such as pressure and internal energy can be directly calculated.

In our KSMD simulations, we have employed the Γ point ($\mathbf{k} = 0$) sampling of the Brillouin zone. We used either 32 or 64 Si atoms (depending on density) in a cubic cell with a periodic boundary condition. The cubic cell size is determined from the mass density. The PAW potential of Si included 12 active electrons; the plane-wave cutoff energy was set to 2000 eV. In all KSMD simulations, a sufficient number of bands (varying from 500 to 4100) were included such that the occupation of the highest band was less than 10^{-5}. The time step varied from $\delta t = 1.5$ fs to $\delta t = 0.085$ fs, respectively, for the lowest and highest densities ($\rho_{min} = 0.1$ g/cm^3 and $\rho_{max} = 50$ g/cm^3). Good convergence was obtained for these parameter sets. The sampled temperature points varied from $T = 2000$ K to a maximum temperature of $T = 500,000$ K. Outside these density and temperature ranges, we switched to the OFMD calculations since the 1s-core electrons must be included in the EOS calculations.

The OFMD method[41] originated from the true spirit of the Hohenberg–Kohn theorem,[46] i.e., the free energy of an electron–ion system at any ion configuration can be written as a function of the electron density. The kinetic energy of the electrons is currently represented by the Thomas–Fermi functional plus the von Weizsäcker correction that takes into account the gradient of electron density. These terms were obtained from the semiclassical expansion of the partition function up to the first order. In OFMD simulations, all electrons, both bound and free, are treated equally. The divergence of the electron-nucleus potential is regularized for each thermodynamic condition through a similar procedure of generating the norm-conserving pseudopotential as the PAW treatment. The cutoff radius is chosen to be less than 10% of the Wigner–Seitz radius to avoid an overlap of regularized ion spheres. The exchange-correlation function is expressed in the local density approximation of Perdew and Zunger.[47]

At each time step of an OFMD simulation, the electron free energy for an ionic configuration is first minimized in terms of the local electron density. Then, the classical ions are moved by the combined electronic and ionic forces, the same as in the KSMD procedure. In our OFMD simulations of silicon plasmas, we used 128 atoms in a cubic cell with periodic boundary conditions. The time step varied from $\delta t = 0.144$ fs to $\delta t = 6 \times 10^{-5}$ fs, respectively, for the lowest-density/lowest-temperature ($\rho = 0.001$ g/cm^3 and $T = 125,000$ K) point and

the highest-density/highest-temperature ($\rho = 500$ g/cm^3 and $T = 10^8$ K) point. Finally, the thermodynamic EOS quantities were statistically evaluated from the molecular-dynamics (MD) propagation of the system (5000 to 100,000 steps, depending on the density).

For each isochoric curve, we examined the EOS quantities for the overlapping temperature points between the KSMD and OFMD calculations. We made the transition from KSMD to OFMD at the temperature point where their differences were the smallest (within ~1%). Carrying out these calculations for a wide range of silicon plasma conditions, we obtained both pressure and internal energies for all the sampled density and temperature points ($\rho = 0.001$ to 500 g/cm^3 and $T = 2000$ to 10^8 K). As an example, in Fig. 149.14 we plot the total pressures as a function of the silicon plasma temperature for each of the sampled isochoric curves.
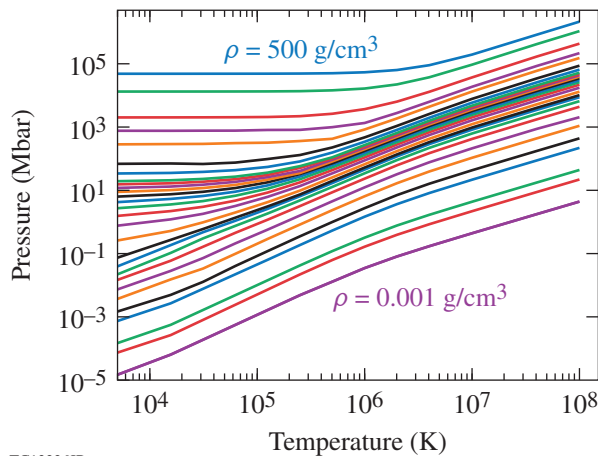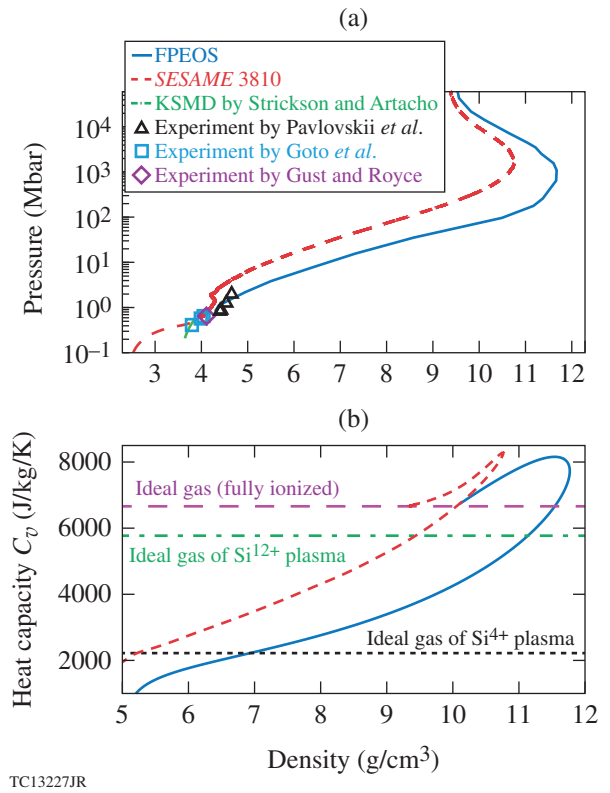

Figure 149.14
Silicon pressure as a function of temperature for all densities ($\rho = 0.001$ to 500 g/cm^3) scanned by our first-principles (KSMD + OFMD) calculations.

Comparison Between FPEOS and *SESAME* EOS

From the FPEOS table, we can derive the principal Hugoniot curve for silicon shocks by using the Rankine–Hugoniot equation. The initial state is chosen to be solid silicon ($\rho_0 = 2.329$ g/cm^3) in its diamond phase at ambient pressure ($P_0 = 1$ bar). We compare the FPEOS Hugoniot with the one derived from the extensively used *SESAME*-EOS model (*SESAME* 3810 table) in Fig. 149.15(a), in which the Hugoniot pressure spanning more than five orders of magnitude is plotted as a function of the shock density. The *SESAME*-EOS model was based on the chemical picture of matter, meaning that the total free energy can be decomposed into the cold curve, the ionic excitation, and the electron thermal excitation. It was typically

Figure 149.15
(a) The shock Hugoniot of silicon predicted by FPEOS (solid blue line) is compared to the EOS-model *SESAME* 3810 (dashed red line), a recent KSMD study (dashed green line),[28] and available experiments (various symbols) by Pavlovskii *et al.*,[16] Gust and Royce,[17] and Goto *et al.*[18] (b) A comparison of heat capacity calculated from FPEOS and *SESAME* 3810 along the principal Hugoniot. Diamond-phase silicon ($\rho_0 = 2.329$ g/cm^3) is chosen as the initial state for the Hugoniot calculations.

constructed (constrained) by the best-available experimental data (typically limited). Specifically, for *SESAME* 3810 (Si) constructed in 1997, the EOS below the solid–liquid phase transition was based on experimental Hugoniot data.[16–18] For conditions above the liquid phase transition, the EOS was constructed such that the shock Hugoniot was "similar" to germanium (*SESAME* 3950) up to 4.4 Mbar. The ion thermal contribution is based on a Debye model with a correction for the liquid's specific heat beyond the melt temperature.[48] The correction also ensures that in the high-temperature limit, the proper model (ideal gas) that is recovered will give a shock Hugoniot compression ratio $\rho/\rho_0 = 4$. The Hugoniot comparison in Fig. 149.15(a) indicates that under shock compression, silicon is much softer than predicts by the traditional chemical picture of materials.[29] For example, at a constant pressure of ~20 Mbar, the *SESAME* 3810 table predicts a shock density of $\rho \simeq 6.3$ g/cm^3, while the FPEOS table gives a much-higher

shock density of $\rho \simeq 7.7$ g/cm^3. Namely, the FPEOS table predicts that silicon under 10- to 1000-Mbar pressures is ~20% softer than *SESAME* 3810. For the same shock density at $\rho = 8$ g/cm^3, the *SESAME* 3810 model predicts a shock pressure of $P \simeq 73.4$ Mbar, which is more than 3× higher than the FPEOS case ($P \simeq 24$ Mbar). Figure 149.15(a) indicates that the maximum compression (ρ/ρ_0) changes from the *SESAME*-predicted value of ~4.6 to 5.0 in FPEOS. Finally, in the same figure, we have plotted the existing experimental data,[16–18] which are represented by the different symbols. These Hugoniot data were obtained from explosively driven shock experiments. To the best of our knowledge, no published data exist for laser-shock Hugoniot measurements in pressures above 10 Mbar. The opacity of Si for most velocity interferometer system for any reflector (VISAR) laser wavelengths[49] is one of the hurdles for accurate shock measurements in silicon. Nevertheless, it is shown in Fig. 149.15 that the explosively driven shock data up to ~2 Mbar agree well with our calculations, which seems also to indicate the softening of silicon under compression. It is noted that at the measured highest shock density of $\rho = 4.6$ g/cm^3, the *SESAME*-EOS–predicted pressure is at least 2× higher than the experimental value of $P \simeq 2$ Mbar.

To further examine the properties of shocked silicon, we have calculated the heat capacity C_v along its principal Hugoniot. Because C_v is a measure of the energy change with respect to temperature at a fixed volume, it can give some indication of how rapidly the entropy is increasing with temperature in a silicon shock. The obtained C_v results are plotted in Fig. 149.15(b) as a function of the Hugoniot density for both *SESAME* 3810 (dashed red line) and FPEOS (solid blue line). In Fig. 149.15(b), we also plot three horizontal lines to indicate the expected heat capacities for ideal-gas plasmas of three different ionization stages of Si^{4+}, Si^{12+}, and Si^{14+}, respectively. For instance, the lowest dashed black line represents the ideal-gas plasma that includes only Si^{4+} and free electrons without any interactions. Since the electron ionization process acts like a "heat sink" for the system, one expects the heat capacity to increase during the ionization of bound electrons. This is especially true for the innermost shell electrons because of the large energy gaps between the L-shell and K-shell electrons. This is exactly what can be seen in Fig. 149.15(b), where the FPEOS calculation (solid blue line) gives a peak of C_v near the peak compression at $\rho \simeq 11.5$ g/cm^3 [see Fig. 149.15(a)]. After the 1s-electron ionization is completed, the heat capacity approaches the ideal-gas limit (horizontal dashed pink line) as a fully ionized Si plasma is formed. The *SESAME* 3810–predicted C_v has a similar trend, but the same value of C_v is reached at a smaller density. In other words, at the same density the FPEOS-predicted C_v is ~50%

lower than the *SESAME* 3810 case, meaning that less entropy increase is expected in FPEOS. By referring to the ideal-gas C_v, one can argue that the same ionization stage is first reached at much-lower densities in *SESAME* 3810 than in FPEOS. Again, all of these features are consistent with the higher compressibility of silicon predicted by FPEOS.

Next, we compare the pressure and internal energy of silicon plasmas for off-Hugoniot conditions between FPEOS (solid blue line) and *SESAME* 3810 (dashed red line) in Figs. 149.16–149.18. Figures 149.16(a) and 149.17(a) show the pressure as a function of plasma temperature, respectively, for silicon densities of $\rho = 5$ g/cm^3 and $\rho = 10$ g/cm^3, while the internal energy comparisons are made in Figs. 149.16(b) and 149.17(b). One sees in Fig. 149.16(a) that the *SESAME* pressure is ~10% lower than FPEOS for temperatures $T < 10^4$ K, but it
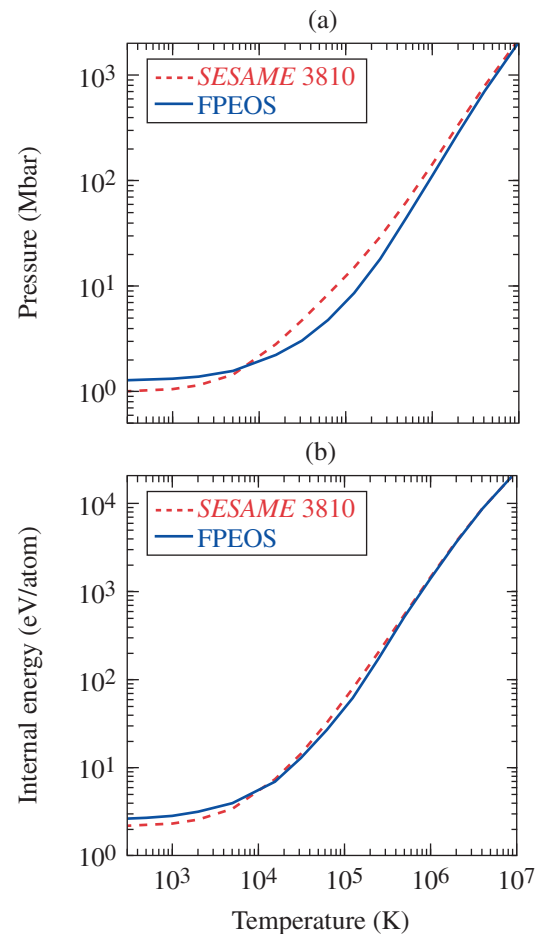

TC13228JR

Figure 149.16
The off-Hugoniot equation-of-state comparisons between FPEOS and *SESAME* 3810. The (a) pressures and (b) internal energies are plotted as functions of temperature for a silicon density of $\rho = 5$ g/cm^3.

reverses for $10^4 < T < 10^6$ K with a "crossover" temperature at $T \sim 10^4$ K (~1 eV). The pressure difference between FPEOS and *SESAME* 3810 reaches a maximum of ~50% in the warm dense regime ($T \sim 10^5$ K) at this density ($\rho = 5$ g/cm^3). This is the regime in which both electron degeneracy and strong ion–ion coupling play significant roles in determining the EOS. The internal energy comparison in Fig. 149.16(b) shows a similar trend, although the difference is only ~20%. For high temperatures of $T > 10^6$ K, both FPEOS and *SESAME* 3810 are in good agreement with each other as the two EOS tables correctly approach the ideal gas limit. Figure 149.17 shows similar EOS comparisons for $\rho = 10$ g/cm^3. At this higher density note that the crossover temperature now moves to near

~10^5 K (~10 eV), and the maximum difference in pressure between FPEOS and *SESAME* 3810 reduces to ~20%. The difference in internal energy in Fig. 149.17(b) is also reduced when compared to Fig. 149.16(b).

Finally, we explore two other isochores at high densities of $\rho = 50$ g/cm^3 and $\rho = 500$ g/cm^3, respectively, in Figs. 149.18(a) and 149.18(b). Again, the two panels compare the pressures of FPEOS with *SESAME* 3810 at various temperatures. Figure 149.18(b) indicates that both FPEOS and *SESAME* 3810 are very close to each other at this high density of $\rho = 500$ g/cm^3, even though *SESAME* 3810 gives a slightly higher pressure over the entire temperature range (no more crossover is seen between
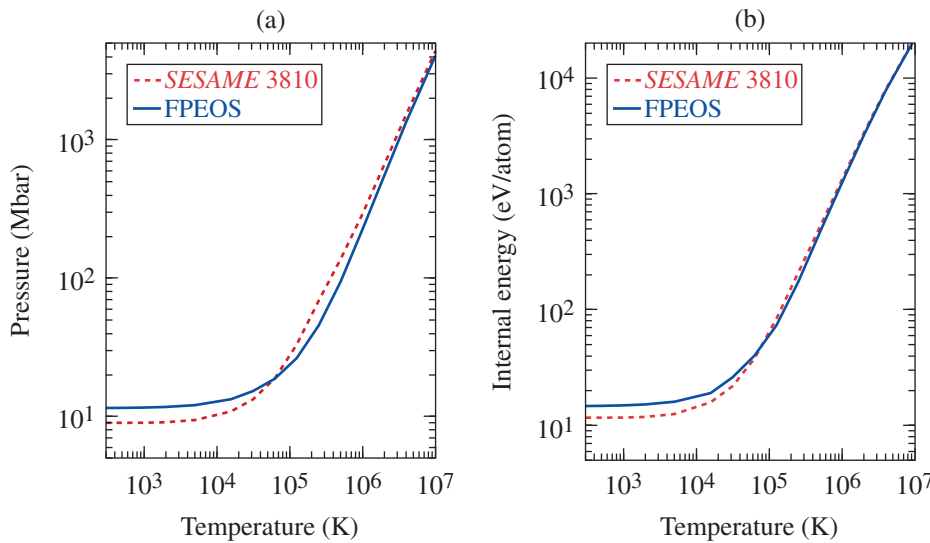

TC13229JR

Figure 149.17
Same as Fig. 149.16 except for a silicon density of $\rho = 10$ g/cm^3.
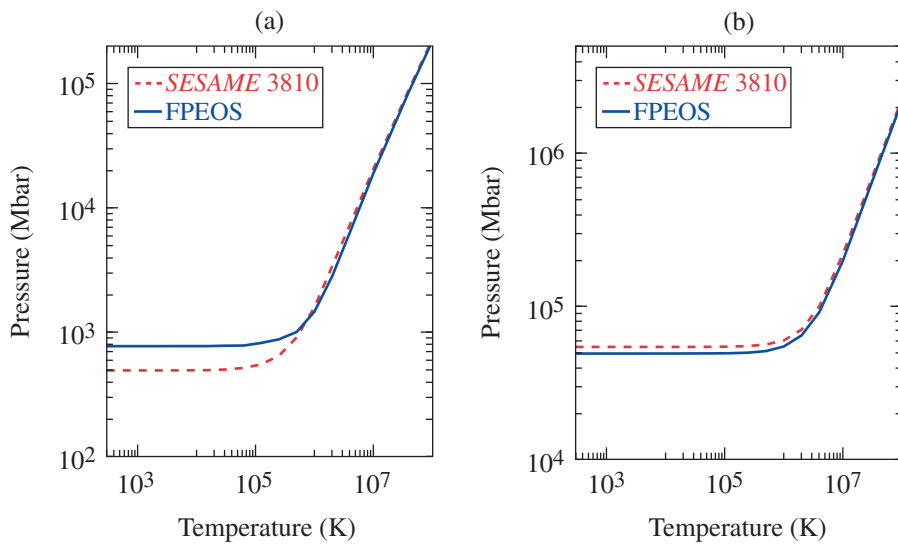

TC13230JR

Figure 149.18
Pressure comparisons between FPEOS and *SESAME* 3810 for higher densities of silicon plasmas: (a) $\rho = 50$ g/cm^3 and (b) $\rho = 500$ g/cm^3.
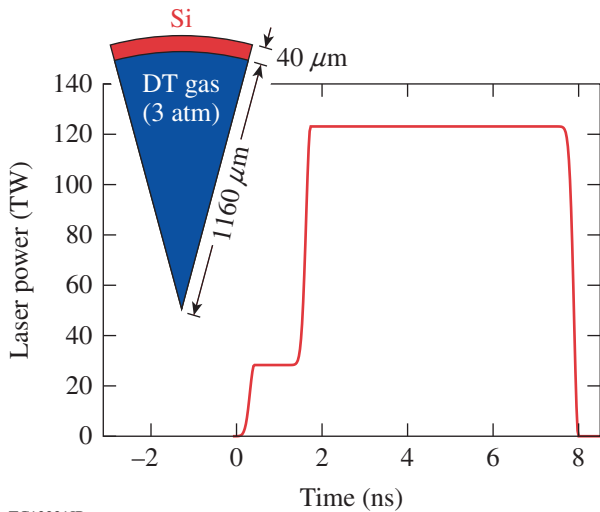
the two EOS's). Both EOS tables are in better agreement with each other in this electron-degeneracy–dominated regime. For the intermediate density of $\rho = 50$ g/cm^3, Fig. 149.18(a) still shows a trend similar to the one seen in Figs. 149.16 and 149.17. Namely, the *SESAME* 3810 model still underestimates the pressure for the low-*T* regime ($T < 10^6$ K). With these large EOS differences identified in both on-Hugoniot and off-Hugoniot warm-dense-plasma conditions, we expect to see significant effects on HED plasma simulations between using the newly established FPEOS and using the *SESAME* 3810 for silicon.

EOS Effects on HED Plasma Simulations Involving Silicon

To examine the EOS effects on HED plasma simulations, we have implemented our FPEOS table of silicon into our radiation–hydrodynamics codes *LILAC* and *DRACO*. We have extrapolated our EOS results for temperatures outside our calculation range (2000 K to 10^8 K). With the implementation of the FPEOS table, we can investigate its effects on HED simulations involving silicon plasmas. Since in an ICF implosion the capsule generally undergoes a path sweeping through many different density and temperature conditions, integrated ICF implosion simulations would be more suitable for examining EOS effects. As an example, we consider a NIF (National Ignition Facility)-type direct-drive implosion with the target and pulse shape shown in Fig. 149.19. The $\phi = 2.4$-mm capsule is made of a 40-μm Si layer filled with 3 atm of deuterium–tritium (DT) gas. The step laser pulse has a total

energy of 800 kJ, with a duration of 8 ns. Figures 149.20–149.23 show the *LILAC* simulation results using either FPEOS (solid blue line) or *SESAME* 3810 (dashed red line) for silicon. Both simulations used the same nonlocal thermal-transport model[50] and inverse-bremsstrahlung absorption with cross-beam energy transfer modeling.[51] For DT gas, the two simulations used the same FPEOS table[52,53] and the same first-principles opacity table[54] of DT, so that the EOS tests solely focused on the silicon ablator layer. In Fig. 149.20, we plot the density and temperature profile snapshot at $t = 0.9$ ns as a function of target radius for the two simulations. At this time, the shock is still propagating inside the Si layer (the shock front is located at $R \sim 1180$ μm). Figure 149.20 indicates that (1) the shock density in FPEOS is ~20% higher than the *SESAME* simulation and (2) the shock in the *SESAME* simulation is ahead of the FPEOS case, giving a shock-speed difference of ~10%. These features can be understood by considering the softening of silicon shock in FPEOS (see Fig. 149.15). Namely, the identical laser drive gives the same ablation pressure in the two simulations; for the same shock pressure (P_s), the FPEOS simulation will give ~20%-higher shock density (ρ_s) as the Hugoniot curve seen in Fig. 149.15(a). Since the shock speed depends on the shock density through $V_s = \sqrt{P_s / \rho_0} / \sqrt{1 - \rho_0 / \rho_s}$, one can see that for the same P_s, the ~20%-higher shock density in FPEOS will give an ~10%-smaller shock speed than the *SESAME* case. Figure 149.20 also indicates that the shock temperature is ~20% higher in FPEOS.
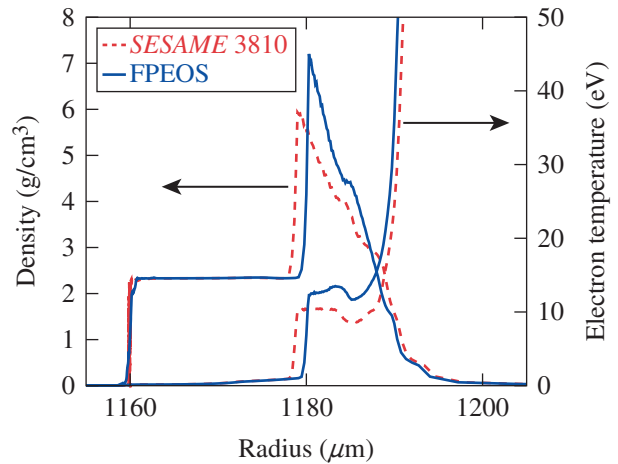

TC13231JR

Figure 149.19
The laser pulse shape and target dimensions for implosion simulations to test the silicon EOS effects. The capsule consists of a 40-μm-thick silicon shell ($\rho_0 = 2.329$ g/cm^3) filled with 3 atm of DT gas. The initial target radius $R = 1200$ μm. The total laser energy is 800 kJ with an 8-ns pulse duration, available at the National Ignition Facility.

TC13232JR

Figure 149.20
Comparisons of density and electron temperature profiles predicted by the two *LILAC* simulations using FPEOS (solid blue lines) and *SESAME* 3810 (dashed red lines) EOS models. The snapshot was taken at $t = 0.9$ ns, when the first shock was still propagating in the silicon layer.
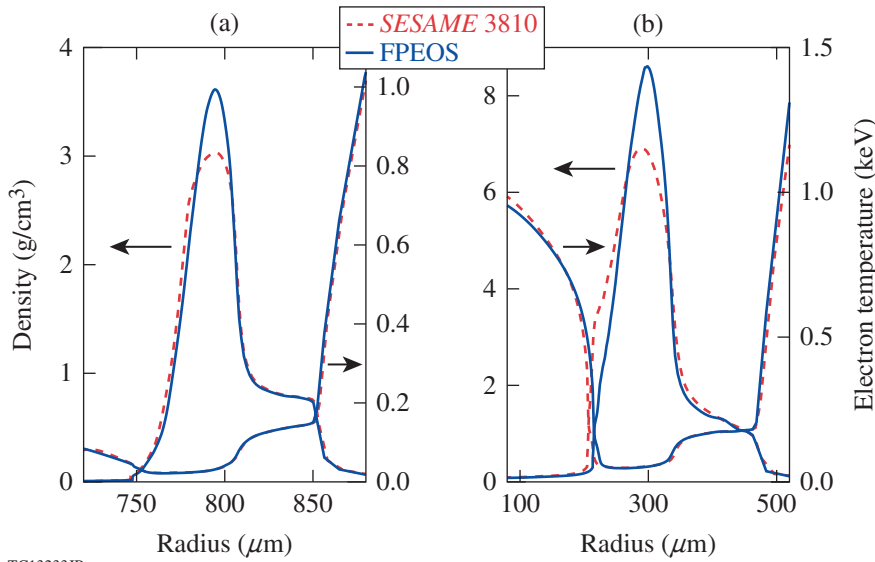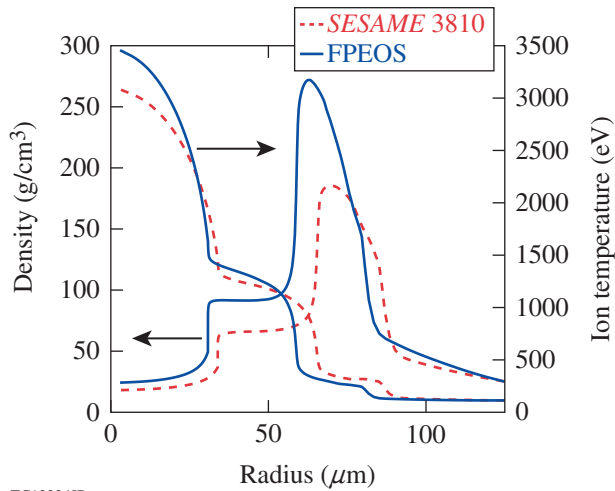
TC13233JR

Figure 149.21
Same as Fig. 149.20 but for different implosion times: (a) $t = 5.4$ ns (in flight of the imploding shell) and (b) $t = 7.9$ ns (the end of shell acceleration).
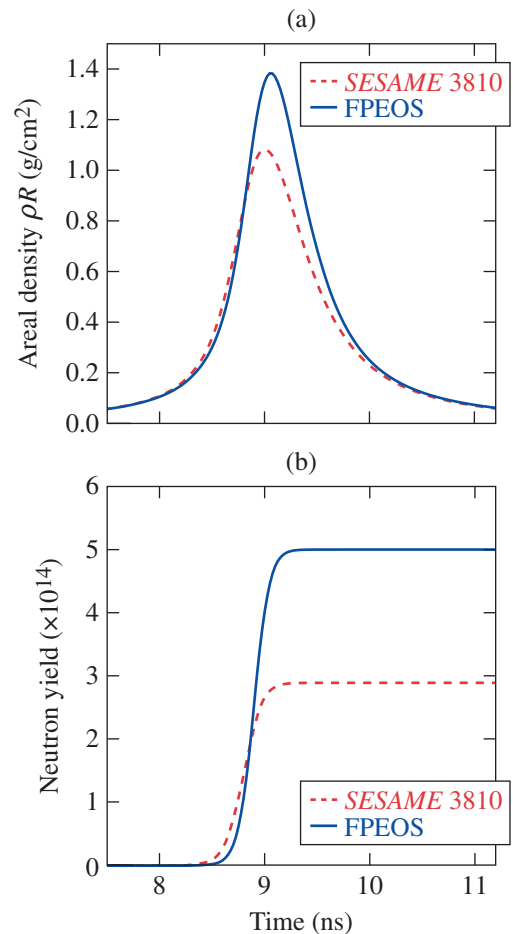

TC13234JR

Figure 149.22
Comparisons of density and ion temperature profiles predicted by the two *LILAC* simulations using FPEOS (solid blue lines) and *SESAME* 3810 (dashed red line) EOS models. Peak neutron production is at $t \sim 9.0$ ns.

TC13235JR

Figure 149.23
Comparisons of (a) the areal density ρR and (b) the total neutron yield as functions of time for the two *LILAC* simulations using FPEOS (solid blue lines) and *SESAME* 3810 (dashed red line) EOS models.

As the implosion proceeds, Fig. 149.21 shows the density and temperature profiles during the in-flight stage of $t = 5.4$ ns [Fig. 149.21(a)] and at the end of acceleration of $t = 7.9$ ns [Fig. 149.21(b)]. One sees from Fig. 149.21 that the peak density of the shell from the FPEOS simulation is always ~20% higher than the *SESAME* 3810 case. This can be attributed to the greater compressibility of silicon predicted by FPEOS. Except for the difference in peak density, the two simulations give very similar density and temperature profiles for the imploding shell. Some difference in the back surface of the shell appears only at the end of the acceleration phase, as indicated by Fig. 149.21(b). Note that the coronal plasma conditions are also very similar

in the two cases, as the EOS difference becomes very small at high temperatures of $T > 10^6$ K. Figure 149.21 also shows an interesting double-ablation-front feature, which can develop in such mid-Z–ablator implosions[55] because of the significant radiation preheat from coronal emissions. The ~20% difference in peak density in the two simulations can have significant consequences when the imploding shell stagnates. Figure 149.22 displays the situation at the time of peak neutron production (near peak compression). Again, the figure shows the density and ion temperature as functions of the target radius. The maximum density reached in the FPEOS simulation is $\rho_p =$ 271.9 g/cm^3, in contrast to the *SESAME* 3810–predicted $\rho_p =$ 185.5 g/cm^3. The Si shell is converged slightly more in FPEOS than *SESAME*, resulting in a somewhat different hot-spot radius ($R_{hs} = 30.5$ μm versus $R_{hs} = 33.6$ μm). Consequently, the maximum ion temperature is increased from $T_i \simeq 3.07$ keV (*SESAME*) to $T_i \simeq 3.45$ keV (FPEOS).

Finally, we plot the history of the compression areal density (ρR) and neutron yield, respectively, in Figs. 149.23(a) and 149.23(b) for the two implosion simulations. One sees from Fig. 149.23(a) that the peak areal density reaches a value of $\rho R = 1.38$ g/cm^2 in FPEOS, which is ~30% higher than the *SESAME* simulation. The total neutron yield predicted by FPEOS, shown by Fig. 149.23(b), is increased by more than ~70% with respect to the *SESAME* case [$Y = 5.0 \times 10^{14}$ (FPEOS) versus $Y = 2.9 \times 10^{14}$ (*SESAME*)]. As a result, the EOS difference can have significant consequences on predicting the 1-D target performance. This illustrates the importance of having a more-accurate EOS table to the 1-D hydrodynamic designs of ICF/HED experiments.

Conclusion

We have applied DFT-based molecular-dynamics simulation methods to investigate the EOS of silicon, spanning a wide range of plasma conditions from $\rho = 0.001$ to 500 g/cm^3 and $T = 2000$ to 10^8 K. The resulting pressures and internal energies have been assembled into a first-principles equation-of-state table, which is studied in detail by comparing it with the extensively used *SESAME* 3810 table of silicon. We found that the shock Hugoniot of silicon is ~20% softer in FPEOS than *SESAME* 3810. For off-Hugoniot warm-dense-plasma conditions, the pressure difference can reach ~50% between FPEOS and *SESAME* 3810, while the internal energy difference is within ~20%. After implementing the FPEOS table of silicon into our 1-D radiation–hydrodynamics code *LILAC*, we tested its effects on HED plasma simulation by carrying out hydro-simulations of an ICF implosion with a Si shell using

either FPEOS or *SESAME* 3810. The simulation results showed (a) the FPEOS-predicted shock density is ~20% higher than the *SESAME* 3810 case (accordingly, the shock speed is ~10% lower in the former case); (b) the peak density of the imploding Si shell is ~20% larger in FPEOS than in *SESAME*; (c) the maximum density at peak compression is higher by ~40%; and (d) the final areal density and yield predicted by FPEOS are respectively higher by ~30% and ~70%, with respect to the *SESAME* simulation. The observed differences in target performance can be attributed to the different compressibility of silicon predicted by FPEOS. These studies illustrate the importance of having a more-accurate EOS table in order to precisely design ICF/HED experiments. Hopefully these results will facilitate shock-wave experiments in the untested high-pressure (>10-Mbar) regime.

REFERENCES

1. G. J. Cheng *et al.*, J. Manuf. Sci. Eng. **130**, 011008 (2008).

2. Y. Zhang *et al.*, Geophys. Res. Lett. **41**, 4554 (2014).

3. H. Sai *et al.*, Appl. Phys. Lett. **106**, 213902 (2015).

4. A. Benuzzi-Mounaix *et al.*, Phys. Scr. **2014**, 014060 (2014).

5. W. D. Langer and A. E. Glassgold, Astrophys. J. **352**, 123 (1990).

6. P. Schilke *et al.*, Astron. Astrophys. **321**, 293 (1997).

7. M. J. Edwards, J. D. Lindl, B. K. Spears, S. V. Weber, L. J. Atherton, D. L. Bleuel, D. K. Bradley, D. A. Callahan, C. J. Cerjan, D. Clark, G. W. Collins, J. E. Fair, R. J. Fortner, S. H. Glenzer, S. W. Haan, B. A. Hammel, A. V. Hamza, S. P. Hatchett, N. Izumi, B. Jacoby, O. S. Jones, J. A. Koch, B. J. Kozioziemski, O. L. Landen, R. Lerche, B. J. MacGowan, A. J. MacKinnon, E. R. Mapoles, M. M. Marinak, M. Moran, E. I. Moses, D. H. Munro, D. H. Schneider, S. M. Sepke, D. A. Shaughnessy, P. T. Springer, R. Tommasini, L. Bernstein, W. Stoeffl, R. Betti, T. R. Boehly, T. C. Sangster, V. Yu. Glebov, P. W. McKenty, S. P. Regan, D. H. Edgell, J. P. Knauer, C. Stoeckl, D. R. Harding, S. Batha, G. Grim, H. W. Herrmann, G. Kyrala, M. Wilke, D. C. Wilson, J. Frenje, R. Petrasso, K. Moreno, H. Huang, K. C. Chen, E. Giraldez, J. D. Kilkenny, M. Mauldin, N. Hein, M. Hoppe, A. Nikroo, and R. J. Leeper, Phys. Plasmas **18**, 051003 (2011).

8. R. L. McCrory, R. Betti, T. R. Boehly, D. T. Casey, T. J. B. Collins, R. S. Craxton, J. A. Delettrez, D. H. Edgell, R. Epstein, J. A. Frenje, D. H. Froula, M. Gatu-Johnson, V. Yu. Glebov, V. N. Goncharov, D. R. Harding, M. Hohenberger, S. X. Hu, I. V. Igumenshchev, T. J. Kessler, J. P. Knauer, C. K. Li, J. A. Marozas, F. J. Marshall, P. W. McKenty, D. D. Meyerhofer, D. T. Michel, J. F. Myatt, P. M. Nilson, S. J. Padalino, R. D. Petrasso, P. B. Radha, S. P. Regan, T. C. Sangster, F. H. Séguin, W. Seka, R. W. Short, A. Shvydky, S. Skupsky, J. M. Soures, C. Stoeckl, W. Theobald, B. Yaakobi, and J. D. Zuegel, Nucl. Fusion **53**, 113021 (2013).

9. R. S. Craxton, K. S. Anderson, T. R. Boehly, V. N. Goncharov, D. R. Harding, J. P. Knauer, R. L. McCrory, P. W. McKenty, D. D. Meyerhofer, J. F. Myatt, A. J. Schmitt, J. D. Sethian, R. W. Short, S. Skupsky, W. Theobald, W. L. Kruer, K. Tanaka, R. Betti, T. J. B. Collins, J. A. Delettrez, S. X. Hu, J. A. Marozas, A. V. Maximov, D. T. Michel, P. B. Radha, S. P. Regan, T. C. Sangster, W. Seka, A. A. Solodov, J. M. Soures, C. Stoeckl, and J. D. Zuegel, Phys. Plasmas **22**, 110501 (2015).

10. S. W. Haan *et al.*, Phys. Plasmas **18**, 051001 (2011).

11. S. X. Hu, G. Fiksel, V. N. Goncharov, S. Skupsky, D. D. Meyerhofer, and V. A. Smalyuk, Phys. Rev. Lett. **108**, 195003 (2012).

12. G. Fiksel, S. X. Hu, V. N. Goncharov, D. D. Meyerhofer, T. C. Sangster, V. A. Smalyuk, B. Yaakobi, M. J. Bonino, and R. Jungquist, Phys. Plasmas **19**, 062704 (2012).

13. S. X. Hu, D. T. Michel, D. H. Edgell, D. H. Froula, R. K. Follett, V. N. Goncharov, J. F. Myatt, S. Skupsky, and B. Yaakobi, Phys. Plasmas **20**, 032704 (2013).

14. J. F. Myatt, H. X. Vu, D. F. DuBois, D. A. Russell, J. Zhang, R. W. Short, and A. V. Maximov, Phys. Plasmas **20**, 052705 (2013).

15. V. N. Goncharov, T. C. Sangster, R. Betti, T. R. Boehly, M. J. Bonino, T. J. B. Collins, R. S. Craxton, J. A. Delettrez, D. H. Edgell, R. Epstein, R. K. Follet, C. J. Forrest, D. H. Froula, V. Yu. Glebov, D. R. Harding, R. J. Henchen, S. X. Hu, I. V. Igumenshchev, R. Janezic, J. H. Kelly, T. J. Kessler, T. Z. Kosc, S. J. Loucks, J. A. Marozas, F. J. Marshall, A. V. Maximov, R. L. McCrory, P. W. McKenty, D. D. Meyerhofer, D. T. Michel, J. F. Myatt, R. Nora, P. B. Radha, S. P. Regan, W. Seka, W. T. Shmayda, R. W. Short, A. Shvydky, S. Skupsky, C. Stoeckl, B. Yaakobi, J. A. Frenje, M. Gatu-Johnson, R. D. Petrasso, and D. T. Casey, Phys. Plasmas **21**, 056315 (2014).

16. M. N. Pavlovskii, Sov. Phys.-Solid State **9**, 2514 (1968).

17. W. H. Gust and E. B. Royce, J. Appl. Phys. **42**, 1897 (1971).

18. T. Goto, T. Sato, and Y. Syono, Jpn. J. Appl. Phys. **21**, L369 (1982).

19. L. Loveridge-Smith, A. Allen, J. Belak, T. Boehly, A. Hauer, B. Holian, D. Kalantar, G. Kyrala, R. W. Lee, P. Lomdahl, M. A. Meyers, D. Paisley, S. Pollaine, B. Remington, D. C. Swift, S. Weber, and J. S. Wark, Phys. Rev. Lett. **86**, 2349 (2001).

20. P. Celliers, A. Ng, G. Xu, and A. Forsman, Phys. Rev. Lett. **68**, 2305 (1992).

21. A. Ng, P. Celliers, G. Xu, and A. Forsman, Phys. Rev. E **52**, 4299 (1995).

22. Th. Löwer *et al.*, Phys. Rev. Lett. **80**, 4000 (1998).

23. E. J. Reed, J. D. Joannopoulos, and L. E. Fried, AIP Conf. Proc. **620**, 343 (2002).

24. I. I. Oleynik *et al.*, AIP Conf. Proc. **845**, 413 (2006).

25. G. Mogni *et al.*, Phys. Rev. B. **89**, 064104 (2014).

26. D. C. Swift *et al.*, Phys. Rev. B **64**, 214107 (2001).

27. B. Militzer and K. P. Driver, Phys. Rev. Lett. **115**, 176403 (2015).

28. O. Strickson and E. Artacho, Phys. Rev. B **93**, 094107 (2016).

29. S. X. Hu, B. Militzer, L. A. Collins, K. P. Driver, and J. D. Kress, Phys. Rev. B **94**, 094109 (2016).

30. B. I. Bennett *et al.*, Los Alamos National Laboratory, Los Alamos, NM, Report LA-7130 (1978).

31. R. M. More *et al.*, Phys. Fluids **31**, 3059 (1988).

32. J. Delettrez, R. Epstein, M. C. Richardson, P. A. Jaanimagi, and B. L. Henke, Phys. Rev. A **36**, 3926 (1987).

33. L. Collins *et al.*, Phys. Rev. E **52**, 6202 (1995).

34. J. G. Clérouin and S. Bernard, Phys. Rev. E **56**, 3534 (1997).

35. L. A. Collins *et al.*, Phys. Rev. B **63**, 184110 (2001).

36. M. P. Desjarlais, Phys. Rev. B **68**, 064204 (2003).

37. C. Pierleoni *et al.*, Phys. Rev. Lett. **73**, 2145 (1994).

38. R. C. Clay *et al.*, Phys. Rev. B **93**, 035121 (2016).

39. S. Root *et al.*, Phys. Rev. Lett. **115**, 198501 (2015).

40. W. Kohn and L. J. Sham, Phys. Rev. **140**, A1133 (1965).

41. F. Lambert, J. Clérouin, and G. Zérah, Phys. Rev. E **73**, 016403 (2006).

42. G. Kresse and J. Hafner, Phys. Rev. B **47**, 558 (1993).

43. G. Kresse and J. Hafner, Phys. Rev. B **49**, 14,251 (1994).

44. G. Kresse and J. Furthmüller, Phys. Rev. B **54**, 11,169 (1996).

45. J. P. Perdew, K. Burke, and M. Ernzerhof, Phys. Rev. Lett. **77**, 3865 (1996); **78**, 1396(E) (1997).

46. P. Hohenberg and W. Kohn, Phys. Rev. **136**, B864 (1964).

47. J. P. Perdew and A Zunger, Phys. Rev. B **23**, 5048 (1981).

48. J. D. Johnson, High Press. Res. **6**, 277 (1991).

49. P. M. Celliers, G. W. Collins, L. B. Da Silva, D. M. Gold, R. Cauble, R. J. Wallace, M. E. Foord, and B. A. Hammel, Phys. Rev. Lett. **84**, 5564 (2000).

50. V. N. Goncharov, T. C. Sangster, P. B. Radha, R. Betti, T. R. Boehly, T. J. B. Collins, R. S. Craxton, J. A. Delettrez, R. Epstein, V. Yu. Glebov, S. X. Hu, I. V. Igumenshchev, J. P. Knauer, S. J. Loucks, J. A. Marozas, F. J. Marshall, R. L. McCrory, P. W. McKenty, D. D. Meyerhofer, S. P. Regan, W. Seka, S. Skupsky, V. A. Smalyuk, J. M. Soures, C. Stoeckl, D. Shvarts, J. A. Frenje, R. D. Petrasso, C. K. Li, F. Séguin, W. Manheimer, and D. G. Colombant, Phys. Plasmas **15**, 056310 (2008).

51. I. V. Igumenshchev, D. H. Edgell, V. N. Goncharov, J. A. Delettrez, A. V. Maximov, J. F. Myatt, W. Seka, A. Shvydky, S. Skupsky, and C. Stoeckl, Phys. Plasmas **17**, 122708 (2010).

52. S. X. Hu, B. Militzer, V. N. Goncharov, and S. Skupsky, Phys. Rev. Lett. **104**, 235003 (2010).

53. S. X. Hu, B. Militzer, V. N. Goncharov, and S. Skupsky, Phys. Rev. B **84**, 224109 (2011).

54. S. X. Hu, L. A. Collins, V. N. Goncharov, T. R. Boehly, R. Epstein, R. L. McCrory, and S. Skupsky, Phys. Rev. E **90**, 033111 (2014).

55. M. Lafon, R. Betti, K. S. Anderson, T. J. B. Collins, R. Epstein, P. W. McKenty, J. F. Myatt, A. Shvydky, and S. Skupsky, Phys. Plasmas **22**, 032703 (2015).